

QUASAR SPECTRUM CLASSIFICATION WITH PRINCIPAL COMPONENT ANALYSIS (PCA): EMISSION LINES IN THE $\text{Ly}\alpha$ FOREST

NAO SUZUKI

Center for Astrophysics and Space Sciences, University of California, San Diego, 9500 Gilman Drive,
 La Jolla, CA 92093-0424; suzuki@genesis.ucsd.edu

Received 2005 March 10; accepted 2005 October 28

ABSTRACT

We investigate the variety in quasar UV spectra ($\lambda\lambda 1020\text{--}1600$), with emphasis on the weak emission lines in the $\text{Ly}\alpha$ forest region, using principal component analysis (PCA). We use 50 smooth continuum-fitted quasar spectra ($0.14 < z < 1.04$) taken by the *Hubble Space Telescope* (HST) Faint Object Spectrograph. The first, second, and third principal component spectra (PCS) account for 63.4%, 14.5%, and 6.2% of the variance, respectively, and the first seven PCS account for 96.1% of the total variance. Three weak emission lines in the $\text{Ly}\alpha$ forest are identified as $\text{Fe II } \lambda 1070.95$, $\text{Fe II} + \text{Fe III } \lambda 1123.17$, and $\text{C III}^* \lambda 1175.88$. Using the first two standardized PCS coefficients, we introduce five classifications. By actively using PCS, we can generate artificial quasar spectra that are useful in testing the detection of quasars, DLAs, and the continuum calibration. We show that the power-law–extrapolated continuum is inadequate to perform precise measurements of the mean flux in the $\text{Ly}\alpha$ forest because of the weak emission lines and the extended tails of $\text{Ly}\alpha$ and $\text{Ly}\beta/\text{O VI}$ emission lines. We show that we miss 5.3% of the flux on average, and there are cases where we would miss 14% of the flux. These corrections are essential in the study of the intergalactic medium at high redshift in order to achieve precise measurements of physical properties, cosmological parameters, and the reionization epoch.

Subject headings: intergalactic medium — methods: data analysis — methods: statistical —
 quasars: absorption lines — quasars: emission lines — techniques: spectroscopic

Online material: color figures

1. INTRODUCTION

It is important for the study of quasar absorption lines to understand the shape of the continua in the $\text{Ly}\alpha$ forest from which we study the physical properties of the intergalactic medium (IGM) and extract cosmological parameters (Kirkman et al. 2003; Tytler et al. 2004b). It is the uncertainty of continuum fitting to the $\text{Ly}\alpha$ forest that makes precise measurements difficult (Croft et al. 2002a; Suzuki et al. 2003; Jena et al. 2005). Thus, we wish to have a simple and objective quasar spectrum classification scheme that enables us to describe the global shape of the continuum, as well as the individual emission-line profiles. Principal component analysis (PCA), also known as Karhunen–Loève expansion (Karhunen 1947; Loève 1948), is one of the best methods to carry out such classification (Kendall 1980).

PCA enables one to summarize the information contained in a large data set, and it is widely used in many areas of astronomy (Connolly et al. 1995; Cabanac et al. 2002, and references therein). Francis et al. (1992) applied PCA to quasar spectra using 232 quasar spectra ($1.8 < z < 2.2$; $\lambda\lambda 1150\text{--}2000$) from the Large Bright Quasar Survey (LBQS; Hewett et al. 1995, 2001). They showed that the first three principal components account for 75% of the variance. Boroson & Green (1992) used 87 low-redshift quasar spectra ($z < 0.5$) and showed the anticorrelation between the equivalent width of Fe II and $[\text{O III}]$ and the correlation between the luminosity, the strength of $\text{He II } \lambda 4686$, and the slope index α_{ox} . Boroson (2002) investigated the relation between the first two principal components and the physical properties such as black hole mass, luminosity, and radio activity. Shang et al. (2003) studied 22 low-redshift UV and optical quasar spectra ($z < 0.5$; $\lambda\lambda 1171\text{--}6607$) and showed the relation between the first principal component and the Baldwin effect, which is the anticorrelation between the luminosity and the equivalent width of the C IV emis-

sion line. Yip et al. (2004) applied PCA to the 16,707 Sloan Digital Sky Survey quasar spectra ($0.08 < z < 5.41$; $\lambda\lambda 900\text{--}8000$) and reported that the spectral classification depends on the redshift and luminosity and that there is no compact set of eigenspectra that can describe the majority of variations. They also showed the relationship between eigencoeficients and the Baldwin effect.

In Suzuki et al. (2005, hereafter Paper I) we analyzed 50 continua-fitted quasar spectra taken by the *Hubble Space Telescope* (HST) Faint Object Spectrograph (FOS). Since they are at low redshifts ($0.14 < z < 1.04$), and the $\text{Ly}\alpha$ forest lines are not so dense, we can see and correctly fit the continuum to the spectra. Using PCA, we attempted to predict the continuum level in the $\text{Ly}\alpha$ forest, where the continuum levels are hard to see because of the abundance of the IGM absorptions. Although we succeeded in predicting the shape of the weak emission lines in the $\text{Ly}\alpha$ forest region, our prediction suffers systematic errors of 3%–30%.

The goal of this paper is to explore the variety of quasar UV spectra in the following manner: (1) we clarify the PCA formulation in order to describe quasar UV spectra quantitatively (§ 3) using eigenspectra or the principal component spectra (PCS); (2) we introduce five classes of quasar UV spectra to help us understand the variety of quasar spectra qualitatively (§ 5); (3) we introduce the idea of artificial quasar spectra (§ 4) and (4) the mean flux correction factor δF (§ 6); and (5) we report the identities of three weak emission lines in the $\text{Ly}\alpha$ forest (see Appendix).

2. DATA

We use the same 50 HST FOS spectra from Paper I, and the detailed description is therein. Here we summarize the 50 HST spectra. These 50 quasar spectra are a subset of the 334 high-resolution HST FOS spectra ($R \sim 1300$) collected and calibrated

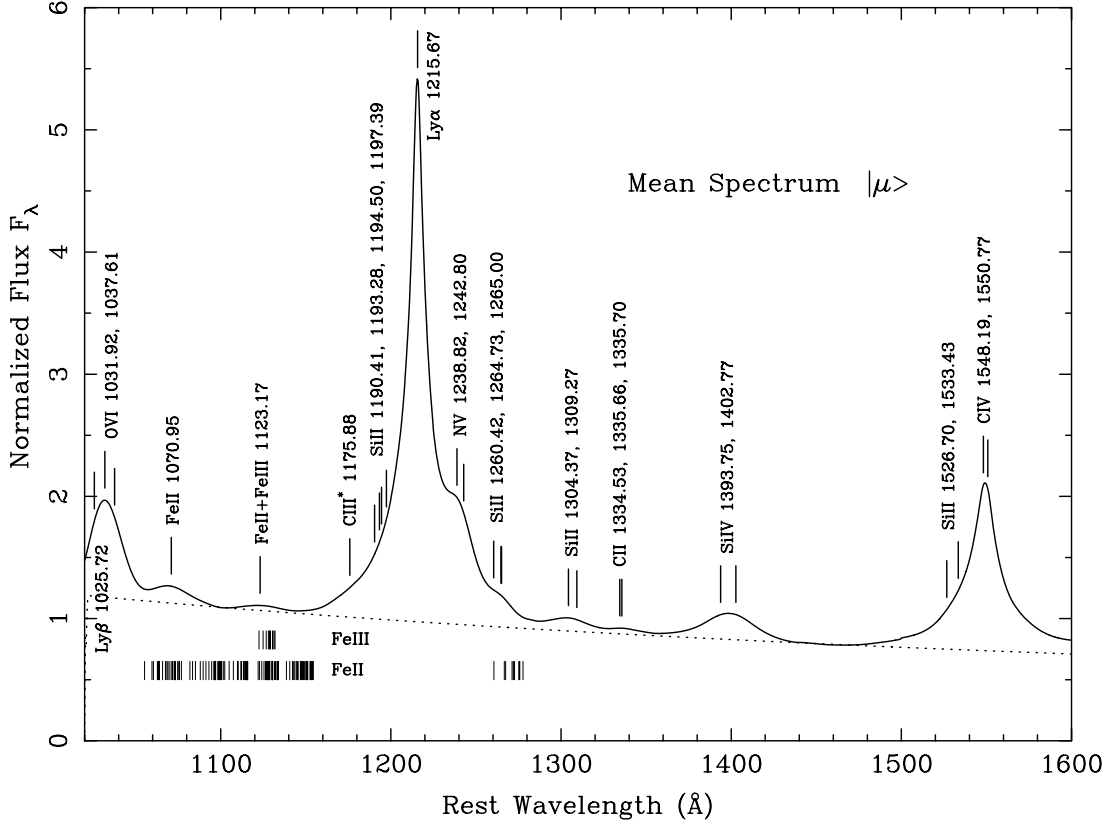


FIG. 1.—Mean spectrum of 50 *HST* quasar spectra. The spectrum is normalized near 1280 Å. The wavelengths are taken from Morton (1991), except for Fe II, Fe III, and C III* lines, which are observed wavelengths from Tytler et al. (2004a). The tick marks shown below the spectrum are the wavelengths of the Fe II and Fe III multiplet. The dotted line is the power-law continuum approximation. Note that the emission lines do exist in the Ly α wavelength region. We also note that the wavelength separation of the Si IV doublet at λ 1400 is relatively large and makes the line profile broad.

by Bechtold et al. (2002), which include all of the *HST* QSO Absorption Line Key Project’s data (Bahcall et al. 1993, 1996; Jannuzi et al. 1996). Bechtold et al. (2002) identified both intergalactic and interstellar medium lines and corrected for Galactic extinction.

For each spectrum, we combined the individual exposures and remeasured the redshift using the peak of the Ly α emission line. Then we brought the spectrum to the rest frame and rebinned it into 0.5 Å pixels. We masked the identified absorption lines and fitted a smooth Chebyshev polynomial curve. We normalized the flux by taking the average of 21 pixels around 1280 Å, where no emission line is seen.

We chose the wavelength range from 1020 to 1600 Å so that we can cover the Ly α forest between the Ly β and the Ly α emission lines while maximizing the number of spectra. We removed broad absorption line (BAL) quasars from the sample since we are interested in emission-line profiles and the continuum shape. Finally, we removed quasars with S/N < 10 per pixel because we cannot extract weak emission-line features in low S/N spectra. The redshift range of the 50 spectra is from 0.14 to 1.04 with a mean of 0.58. The average S/N is 19.5 per 0.5 Å binned pixel.

3. PCA AND PRINCIPAL COMPONENT SPECTRUM

3.1. The PCA Formulation

We express a quasar spectrum in Dirac’s “bra ket” form, $|q_i\rangle$, which is commonly used in quantum mechanics and simplifies our description (Sakurai 1985). We claim that any quasar spectrum, $|q_i\rangle$, is well represented by a reconstructed spectrum, $|r_{i,m}\rangle$,

which is a sum of the mean and the weighted m principal component spectra:

$$|q_i\rangle \sim |r_{i,m}\rangle = |\mu\rangle + \sum_{j=1}^m c_{ij} |\xi_j\rangle \quad (1)$$

where i refers to a quasar, $|\mu\rangle$ is the mean quasar spectrum, $|\xi_j\rangle$ is the j th principal component spectrum (PCS), and c_{ij} is its weight. Unlike in quantum mechanics, the weight, c_{ij} , is not a complex number but a real number.

We found the covariance and correlation matrix of the 50 quasar spectra in Paper I, and by diagonalizing the covariance matrix, we can obtain the PCS. In practice, we found the PCS via a singular value decomposition (SVD) technique from the 50 quasar spectra. The recipes can be found in Francis et al. (1992) and Paper I. Since we defined PCS to be orthonormal,

$$\langle \xi_i | \xi_j \rangle = \delta_{ij}, \quad (2)$$

and we can obtain the weights c_{ij} by calculating the following inner product:

$$c_{ij} = \langle q_i - \mu | \xi_j \rangle. \quad (3)$$

We show the mean spectrum in Figure 1 and the first 10 PCS and the distribution of their weights in Figures 2 and 3.

Although wavelength coverage, normalization, resolution, and the number of quasars are different, the general trend of PCS is similar to that of Francis et al. (1992) with the exception of the

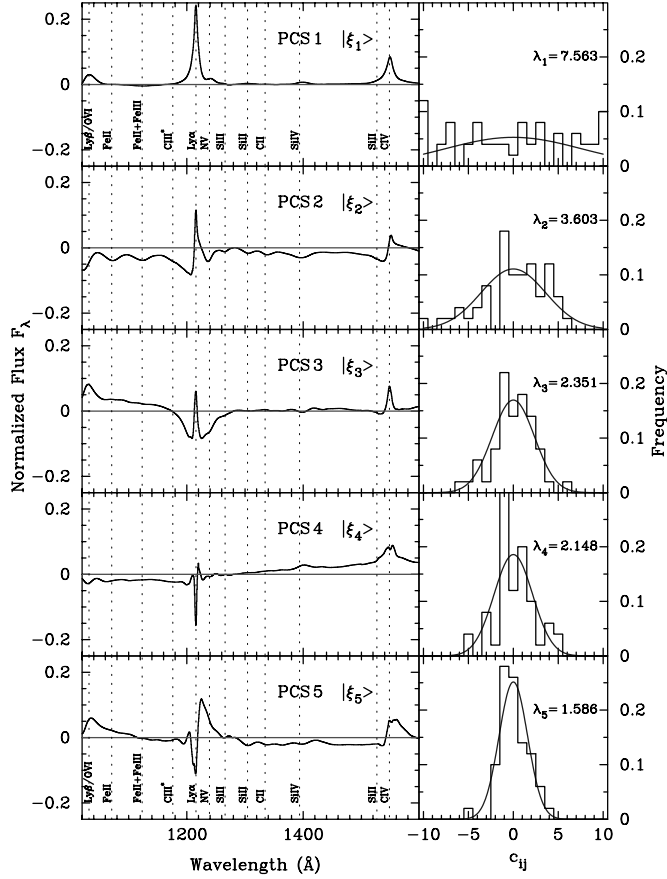


FIG. 2.—The first five PCS (1–5) are shown in the left panels with the distribution of PCS coefficients c_{ij} on the right. The first PCS takes the Ly α , Ly β , and the high-ionization line features (O VI, Si IV, C IV), while the second PCS accounts for the low-ionization lines (Fe II, Fe III, Si II, C II). We expect to have the low-ionization lines in the Ly α forest when a quasar has a negative second PCS coefficient. We note that PCS are designed to be orthonormal. The quasar spectra are normalized near 1280 Å, and every PCS has zero value near 1280 Å. [See the electronic edition of the Supplement for a color version of this figure.]

third PCS. The reason for the exception is that the third PCS of Francis et al. (1992) takes into account BAL features, while we do not have such features since we removed BAL quasars. Our third PCS has sharp emission-line features for Ly β /O VI, the core of Ly α , and C IV emission lines, but broad negative features around the Ly α emission line. The continua of the third, fourth, and fifth PCS have a slope, and the fifth PCS includes the asymmetric feature for the strong emission lines. The fifth PCS is similar to the second PCS in that P Cygni profiles are seen but they are very broad, and there are no low-ionization emission-line features blueward of the Ly α emission line. The sixth and seventh PCS carry some information on low-ionization weak emission lines, but the spectrum features are getting noisy. The eighth and higher order PCS have high-frequency wiggles that no longer correspond to any physical emission lines and are probably due to fitting errors. We used continua-fitted spectra that are free from photon noise, but still they are likely to suffer fitting errors of at least a few percent, as we can see in Figures 7–11 below. The mean spectrum and the first 10 PCS are available online from Paper I. In the next subsection, we discuss the contribution from each PCS quantitatively.

3.2. Quantitative Assessment of PCA Reconstruction

We make use of the residual variance to assess the goodness of the PCA reconstruction. The residual variance of a reconstructed quasar spectrum with m components is a sum of the squares of

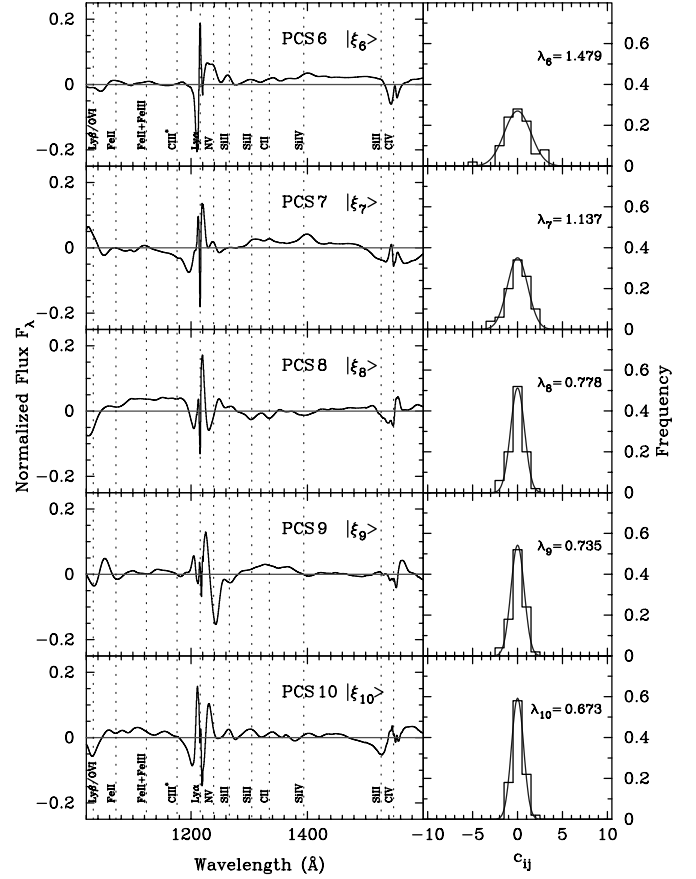


FIG. 3.—Same as Fig. 2, but for the second five PCS (6–10). From eighth and higher PCS, the features in PCS become noisy and no longer have physical correspondence. They are probably fitting errors. [See the electronic edition of the Supplement for a color version of this figure.]

the difference between the quasar spectrum, $|q_i\rangle$, and the reconstructed spectrum, $|r_{i,m}\rangle$:

$$\langle q_i - r_{i,m} | q_i - r_{i,m} \rangle = \sum_{i=m+1}^N c_{ij}^2, \quad (4)$$

where N is the number of quasar spectra.

For the overall contribution from the m th PCS, we define the residual variance fraction, $f(j)$, as follows:

$$f(j) = \frac{\sum_{i=1}^N c_{ij}^2}{\sum_{i,j=1}^N c_{ij}^2}. \quad (5)$$

We redefine the square root of the eigenvalue of the j th PCS as follows:

$$\lambda_j = \frac{1}{N-1} \sqrt{\sum_{i=1}^N c_{ij}^2}. \quad (6)$$

Then we wish to use λ_j to describe the probability distribution function (PDF) of the PCS coefficients. The PDF of the weights is not necessarily a Gaussian, but as shown in Figures 2 and 3, the PDF can be well represented by a Gaussian. We also note that by construction,

$$\sum_{i=1}^N c_{ij} = 0 \quad (7)$$

TABLE 1
EIGENVALUE AND RESIDUAL VARIANCE FRACTION

PARAMETER	COMPONENT j									
	1	2	3	4	5	6	7	8	9	10
Eigenvalue:										
λ_j^2	57.204	12.985	5.528	4.614	2.516	2.189	1.293	0.605	0.541	0.453
λ_j	7.563	3.604	2.351	2.148	1.586	1.479	1.137	0.778	0.735	0.673
Residual variance fraction:										
$f(j)$	0.637	0.145	0.062	0.051	0.028	0.024	0.014	0.007	0.006	0.005
Cumulative	0.637	0.781	0.843	0.894	0.922	0.947	0.961	0.968	0.974	0.979

NOTE.—Cumulative residual variance fraction is a simple sum of residual variance fraction up to the j th PCS.

for any j . Thus, the PDF of weights is characterized by just one parameter, λ_j . The probability of having a weight c_{ij} in an interval $-x_0 \leq c_{ij} \leq x_0$ can be expressed as

$$P(-x_0 \leq c_{ij} \leq x_0) = \int_{-x_0}^{x_0} \frac{1}{\sqrt{2\pi}\lambda_j} e^{-x^2/2\lambda_j^2} dx. \quad (8)$$

Naturally, it would be convenient if we standardize the weight, c_{ij} , by λ_j . We can then rewrite a quasar spectrum as

$$|q_i\rangle \sim |r_{i,m}\rangle = |\mu\rangle + \sum_{j=1}^m \lambda_j \sigma_{ij} |\xi_j\rangle, \quad (9)$$

where the σ_{ij} are the standardized PCS coefficients that represent the deviation from the mean spectrum of the j th PCS of quasar i . The PDF of the σ_{ij} is a normal distribution, so we can immediately tell how far and how different the quasar spectrum would be from the mean spectrum. This standardization of the weights simplifies the discussion of the variety of quasar spectra in § 5.

Another advantage of using λ_j is that we can simplify the residual variance fraction $f(j)$:

$$f(j) = \frac{\lambda_j^2}{\sum_{j=1}^N \lambda_j^2}. \quad (10)$$

The values of $f(j)$ are listed in Table 1. The first, second, and third PCS account for 63.4%, 14.5%, and 6.2% of the variance, respectively. In total, the first three PCS account for 84.3% of the variance of the 50 quasars in our sample. These fractions depend on the normalization and the wavelength coverage. In the literature, Francis et al. (1992) report that the first three PCS account for 75% ($\lambda\lambda 1150-2000$), and Shang et al. (2003) show that the first three PCS carry 80% ($\lambda\lambda 1171-2100$) of the variance. Both groups normalized flux by the mean flux, while this paper normalizes by a flux value near 1280 Å. Our value of 84.3% is slightly higher than the above numbers, probably because we removed the BAL quasars, which are certainly a source of variance. In addition, we used fitted smooth continua to the Ly α forest, while they used the observed raw Ly α forest, which obviously contains a large variance (Tytler et al. 2004b). As shown in Table 1, the contribution from each PCS component to the variance rapidly decreases with order m . It becomes less than 1% after the eighth PCS and then stays the same. With seven PCS components, 96% of the variance has already been accounted for. As is seen in the PCS features in Figure 3, the remaining 4% of the variance is probably due to fitting errors.

4. ARTIFICIAL SPECTRA

We can use PCS to generate artificial spectra. Artificial spectra can be useful in testing the detection of quasars and DLAs, in

flux calibration, in intrinsic quasar flux level fitting, and in cosmological simulations. By assigning PCS coefficients randomly from known PDFs, we can generate artificial quasar spectra. As we have discussed in § 3, the PDF of the j th PCS coefficient is well represented by a Gaussian with a mean of 0 and a standard deviation of λ_j . If we then sum up the PCS with these coefficients (eq. [9]), we can create a set of artificial quasar spectra.

Noiseless quasar spectra are of great use in IGM studies, since at high redshift, it is difficult to see the intrinsic flux level in the Ly α forest. Even at redshift 2, pixels in the Ly α forest hardly reach the flux level with FWHM = 250 km s⁻¹ (Tytler et al. 2004a). Artificial quasar spectra can thus be useful to predict the shape of continuum in the Ly α forest (Paper I) and to calibrate continuum fitting to the Ly α forest (Tytler et al. 2004a, 2004b). They would be also useful to test the detection limit of the high-redshift quasar survey since the Ly α emission can possibly boost the brightness by 0.15 mag. We have generated 10,000 artificial quasar spectra using the first seven PCS for a more realistic representation of the quasar spectra. We concluded that the features seen in PCS greater than eighth are noise, and we did not include higher order PCS. We will provide artificially generated spectra to the community on request.

5. PCA CLASSIFICATION

5.1. Introduction of Five Classes

This paper attempts to classify quasar spectra quantitatively using our standardized PCS coefficients, σ_{ij} . We note that there is no discrete classification of quasar spectra and that they vary continuously. However, this classification will help us in fitting the continua to the Ly α forest spectrum.

We use the first two PCS coefficients to demonstrate the variety of emission lines and continua. We divide the σ_{i1} versus σ_{i2} diagram (Fig. 4) into five zones and introduce five classes of spectral types that enable us to discuss the shape of continua qualitatively. As we have seen in § 3 and Table 1, the first two PCS coefficients account for 77.9% of the variance and represent the overall shape of the quasar spectrum. We introduce polar coordinates as follows:

$$r_i = \sqrt{\sigma_{i1}^2 + \sigma_{i2}^2}, \quad (11)$$

$$\tan \theta_i = \frac{\sigma_{i2}}{\sigma_{i1}}, \quad (12)$$

where r_i represents the deviation from the mean spectrum and the angle θ_i tells us about the profiles of the emission lines.

The main goal of this classification is to differentiate the families of quasar spectra. In practice, when we fit the intrinsic flux level to a quasar spectrum, it would be convenient for us if we could know from which family of the quasar spectrum we should

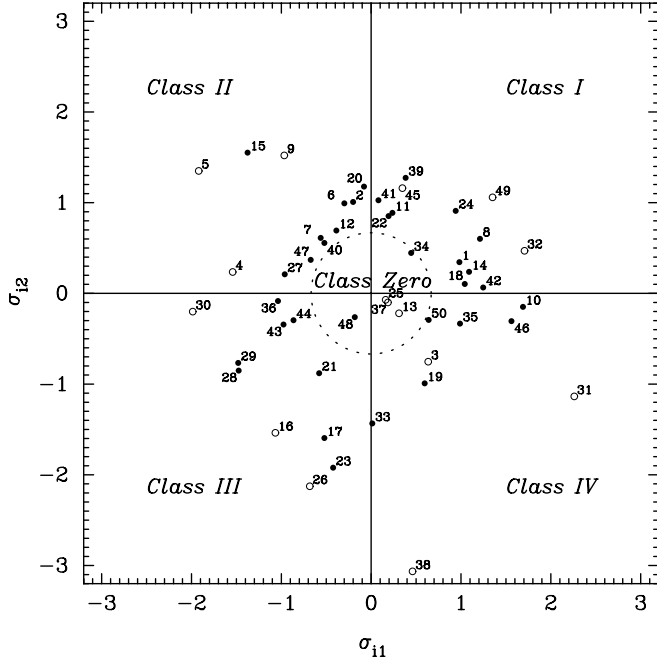


FIG. 4.—Distribution of standardized first two PCS coefficients for 50 quasars. The small number beside each point is quasar number i , which is listed in Table 2. For quasars with open circles, we have quasar spectra shown in Figs. 7–11. We intentionally chose extreme cases to show a wide variety of quasar spectra. The dotted circle has a radius of 0.668. We divide this plane into five zones and define the five classes. We define Class Zero as the quasars that have radius less than or equal to 0.668 and Classes I–IV as the ones that have radius greater than 0.668 and are in quadrants I–IV, respectively.

start with. First, we define “Class Zero” for those close to the mean spectrum in shape. We define Classes I–IV corresponding to the quadrants I–IV in the σ_{i1} versus σ_{i2} diagram, shown in Figure 4. The probability of $r \leq r_0$ is

$$P(r \leq r_0) = \int_0^{r_0} r e^{-r^2/2} dr \quad (13)$$

$$= 1 - e^{-r_0^2/2}. \quad (14)$$

Now, we wish to define the fraction of the five classes to be equal, namely, 0.2 each. We find that $r_0 = 0.668$ gives $P(r \leq r_0) = 0.2$, so we define Class Zero for a quasar spectrum that has $r \leq 0.668$. For quasar spectra with $r > 0.668$, we define the Classes I through IV corresponding to the quadrants first through fourth on the σ_{i1} versus σ_{i2} diagram (Fig. 4).

Our standardized PCS coefficients are plotted on the σ_{i1} versus σ_{i2} diagram in Figure 4, where the dotted circle shows the circle with radius $r_0 = 0.668$. The small numbers noted beside the points are the quasar identification numbers i that are listed in Table 2.

5.2. Demonstration of Five Classes

We show the mean spectrum in Figure 1. By definition the mean spectrum $|\mu\rangle$ has $r = 0$, and naturally it belongs to Class Zero. In Figure 5 we show the artificially generated four classes, I–IV, of the quasar spectra to illustrate their typical spectral shape. They are the sum of the mean and the first two PCS with $\sigma_{i1} = \pm 1$ and $\sigma_{i2} = \pm 1$. The generated four spectra of Classes I–IV

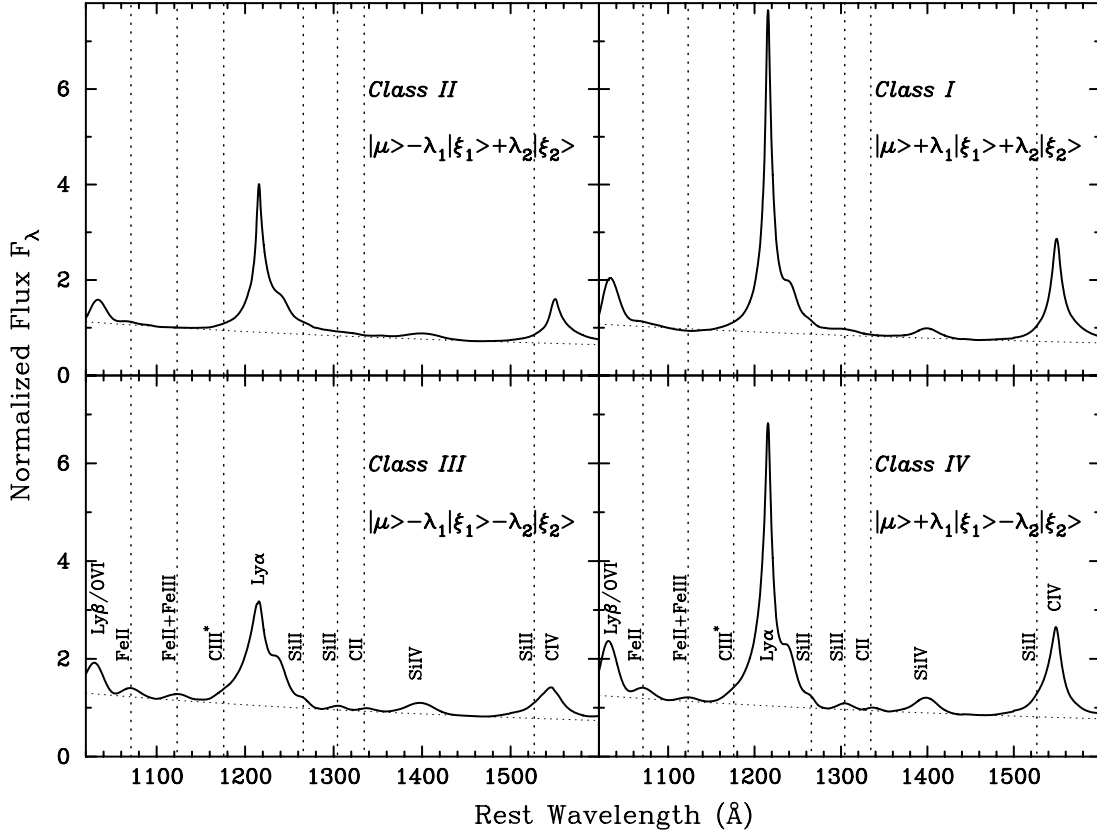


FIG. 5.—Illustration of four classes. We artificially generated these four spectra using the first two PCS. We chose $\pm\sigma_{i1}$ and $\pm\sigma_{i2}$ to generate the four spectra, and an equation is given in the legend in which $|\mu\rangle$ is the mean spectrum, λ_1 and λ_2 are the square roots of the first two eigenvalues, and $|\xi_1\rangle$ and $|\xi_2\rangle$ are the first two PCS. The wavelengths of low-ionization lines are shown as vertical dotted lines. Note that the four spectra are plotted in the same scale, and the emission-line peak contrast with the continuum characterizes the classification. Classes I and II do not have any weak emission lines and the power-law continuum fit (sloped dotted line) is a good approximation of the continuum in the Ly α forest, while Classes III and IV show prominent low-emission lines.

TABLE 2
THE MEAN FLUX CORRECTION FACTOR δF AND EQUIVALENT WIDTH OF EMISSION LINES

i	Quasar	δF	Ly β /O VI $\lambda 1025$	Fe II $\lambda 1071$	Fe III $\lambda 1123$	C III* $\lambda 1176$	Ly α $\lambda 1216$	N V $\lambda 1240$	Si II $\lambda 1263$	Si II $\lambda 1307$	C II $\lambda 1335$	Si IV $\lambda 1397$	C IV $\lambda 1549$
Class Zero ($r \leq 0.668$)													
13.....	Q0947+3940	0.972	8.8	1.4	0.0	0.0	102.9	0.7	0.5	0.0	0.0	13.2	59.8
25.....	Q1229-0207	0.953	9.5	0.9	0.2	0.0	87.7	0.4	0.1	1.8	0.0	6.9	47.4
34.....	Q1424-1150	0.903	9.5	1.1	0.0	0.0	131.9	0.6	0.0	0.0	0.0	8.1	50.4
37.....	Q1538+4745	0.926	8.2	0.4	0.9	0.0	132.9	0.0	0.0	0.4	0.0	6.8	43.4
48.....	Q2340-0339	0.963	5.1	0.3	0.0	0.0	83.5	0.7	0.0	0.0	0.0	5.7	41.5
Average		0.944	8.2	0.8	0.2	0.0	107.8	0.5	0.1	0.4	0.0	8.1	48.5
STD		0.028	1.8	0.5	0.4	0.0	23.6	0.3	0.2	0.8	0.0	2.9	7.2
Class I ($r > 0.668$, $0 \leq \theta < 90^\circ$)													
1.....	Q0003+1553	0.940	8.6	0.1	0.0	0.0	115.7	0.0	0.0	2.2	0.0	6.5	55.2
8.....	Q0439-4319	0.970	13.3	0.0	0.0	0.0	119.2	1.1	0.0	1.2	0.0	7.3	58.0
11.....	Q0637-7513	0.980	15.6	2.5	0.0	0.0	87.2	2.2	0.3	0.0	0.0	8.6	38.9
14.....	Q0953+4129	0.937	12.1	1.9	0.3	0.0	124.2	1.4	0.3	0.0	0.0	10.6	63.6
18.....	Q1007+4147	0.943	11.6	2.0	0.1	0.1	145.4	1.9	0.0	2.0	0.3	10.4	65.5
22.....	Q1137+6604	0.939	10.8	1.8	0.2	0.0	99.2	0.6	0.2	0.6	0.0	7.3	45.1
24.....	Q1216+0655	0.959	9.9	0.9	0.0	0.0	124.7	0.0	0.0	0.6	0.0	8.8	52.4
32.....	Q1354+1933	0.974	10.3	0.2	0.1	0.1	134.6	0.5	0.5	2.0	1.1	7.9	65.5
39.....	Q1622+2352	0.971	9.3	0.7	0.0	0.1	111.3	0.2	0.0	0.0	0.0	7.7	65.2
41.....	Q1821+6419	0.986	13.6	0.3	0.0	0.0	115.3	0.2	0.0	0.0	0.0	7.8	50.6
42.....	Q1928+7351	0.982	10.2	0.0	0.0	0.0	149.4	1.9	0.0	0.0	0.0	12.4	74.3
45.....	Q2243-1222	0.966	8.1	0.3	0.0	0.1	103.2	0.0	0.0	2.2	0.2	8.1	51.6
49.....	Q2344+0914	0.963	13.9	0.8	0.0	0.0	143.1	1.8	0.5	1.6	0.0	5.3	50.9
Average		0.962	11.3	0.9	0.1	0.0	121.0	0.9	0.1	1.0	0.1	8.4	56.7
STD		0.017	2.3	0.9	0.1	0.0	18.7	0.8	0.2	0.9	0.3	1.9	9.8
Class II ($r > 0.668$, $90^\circ \leq \theta < 180^\circ$)													
2.....	Q0026+1259	0.950	9.6	2.4	0.1	0.0	92.1	3.6	0.1	0.0	0.0	9.2	19.4
4.....	Q0159-1147	0.948	2.8	0.3	0.9	0.0	52.8	1.0	0.0	1.1	0.8	4.2	16.8
5.....	Q0349-1438	0.974	1.8	0.0	0.0	0.1	54.9	0.0	0.0	0.0	0.0	4.0	28.0
6.....	Q0405-1219	0.950	6.9	0.7	1.1	0.0	92.5	0.4	0.0	1.1	0.0	6.5	35.0
7.....	Q0414-0601	0.958	6.1	0.0	0.1	0.0	114.0	0.9	0.0	0.0	0.0	5.1	40.1
9.....	Q0454-2203	0.935	11.6	4.2	0.0	0.0	105.7	2.2	0.3	1.1	0.0	7.2	33.9
12.....	Q0923+3915	0.973	7.2	0.0	0.1	0.0	95.1	0.1	0.0	1.2	0.0	5.1	46.4
15.....	Q0954+5537	0.983	3.3	0.0	0.4	0.1	42.6	0.3	1.1	0.0	0.0	1.9	17.9
20.....	Q1104+1644	0.958	5.7	0.7	0.0	0.0	104.5	0.0	0.0	0.5	0.0	7.8	54.1
27.....	Q1252+1157	0.939	6.1	2.7	2.4	0.0	72.7	1.0	0.2	0.0	0.5	6.0	25.5
40.....	Q1637+5726	0.945	4.5	0.9	0.2	0.0	77.6	0.7	0.0	0.3	0.0	5.4	33.2
47.....	Q2251+1552	1.015	7.1	2.3	0.0	0.0	60.1	1.0	0.0	0.0	0.0	2.6	23.2
Average		0.960	6.1	1.2	0.4	0.0	80.4	0.9	0.1	0.4	0.1	5.4	31.1
STD		0.022	2.8	1.4	0.7	0.0	23.7	1.0	0.3	0.5	0.2	2.1	11.6
Class III ($r > 0.668$, $180^\circ \leq \theta < 270^\circ$)													
16.....	Q0959+6827	0.865	3.6	4.0	2.9	0.1	81.0	3.1	0.7	1.3	1.3	12.1	25.2
17.....	Q1001+2910	0.949	3.4	3.4	2.4	0.0	68.7	2.0	0.7	2.9	2.1	9.3	26.2
21.....	Q1115+4042	0.957	7.3	4.3	3.2	0.0	82.3	1.8	0.3	2.5	1.5	8.6	29.7
23.....	Q1148+5454	0.928	3.4	3.9	2.8	0.0	108.4	1.1	0.9	1.8	1.5	14.1	30.8
26.....	Q1248+4007	0.937	2.9	3.0	3.2	0.1	111.6	2.1	0.6	1.6	0.6	12.2	28.6
28.....	Q1259+5918	0.954	2.8	2.5	1.8	0.0	63.5	1.0	1.7	2.7	0.7	10.1	19.8
29.....	Q1317+2743	0.963	3.2	0.8	1.3	0.0	57.2	1.5	0.4	0.5	0.1	7.1	17.9
30.....	Q1320+2925	0.977	1.1	3.9	1.2	0.0	58.6	1.0	0.6	0.4	0.1	5.7	14.4
36.....	Q1444+4047	0.925	4.0	3.0	3.8	0.1	65.0	3.6	0.0	0.3	0.7	9.9	24.0
43.....	Q2145+0643	0.943	1.6	0.0	0.0	0.0	71.3	0.6	0.0	0.0	0.3	1.6	35.9
44.....	Q2201+3131	0.928	4.8	0.6	1.2	0.0	69.9	0.0	0.0	0.0	0.0	7.6	28.8
Average		0.939	3.5	2.7	2.2	0.0	76.1	1.6	0.5	1.3	0.8	8.9	25.6
STD		0.029	1.6	1.5	1.1	0.0	18.5	1.1	0.5	1.1	0.7	3.5	6.2
Class IV ($r > 0.668$, $270^\circ \leq \theta < 360^\circ$)													
3.....	Q0044+0303	0.965	8.6	1.3	0.0	0.0	146.0	1.5	0.1	1.7	0.1	11.3	71.2
10.....	Q0624+6907	0.888	8.2	5.1	3.0	0.0	174.5	3.9	0.6	2.5	1.3	11.3	51.7
19.....	Q1100+7715	0.948	9.7	1.7	0.0	0.0	101.8	1.0	0.0	0.0	0.0	8.5	72.1

TABLE 2—*Continued*

<i>i</i>	Quasar	δF	Ly β /O VI $\lambda 1025$	Fe II $\lambda 1071$	Fe III $\lambda 1123$	C III* $\lambda 1176$	Ly α $\lambda 1216$	N V $\lambda 1240$	Si II $\lambda 1263$	Si II $\lambda 1307$	C II $\lambda 1335$	Si IV $\lambda 1397$	C IV $\lambda 1549$
31.....	Q1322+6557	0.925	8.3	1.8	1.7	0.0	138.5	2.7	0.0	3.3	0.8	9.3	55.5
33.....	Q1402+2609	0.865	6.3	3.1	4.7	0.0	82.0	1.8	0.8	2.3	1.8	5.1	31.7
35.....	Q1427+4800	0.944	13.9	1.8	0.1	0.0	96.9	0.7	0.0	0.6	0.2	16.9	57.3
38.....	Q1544+4855	0.860	2.9	5.7	5.5	0.0	119.5	1.0	1.6	5.1	3.6	16.5	33.5
46.....	Q2251+1120	0.937	10.5	0.8	0.0	0.1	141.6	4.5	0.0	2.1	0.0	7.8	69.8
50.....	Q2352–3414	0.937	9.0	0.8	1.3	0.0	129.4	0.4	0.0	0.7	0.2	6.6	61.8
Average		0.919	8.6	2.4	1.8	0.0	125.6	1.9	0.3	2.0	0.9	10.4	56.1
STD		0.038	3.0	1.8	2.1	0.0	28.7	1.5	0.6	1.6	1.2	4.1	15.1
Total													
Average		0.947	7.5	1.6	0.9	0.0	100.9	1.2	0.3	1.0	0.4	8.1	42.8
STD		0.031	3.7	1.5	1.4	0.0	30.4	1.1	0.4	1.1	0.7	3.3	17.0

have angles θ of 45° , 135° , 225° , and 315° , respectively, and they all have $r = \sqrt{2}$. The four spectra are plotted on the same scale in Figure 5 so that we can see the contrast of the emission lines with the continuum in a uniform manner.

In Figures 7–11 below, we show three observed spectra from each class where we intentionally chose the extreme cases for Classes I–IV. Quasars are plotted at rest-frame wavelengths with the luminosities that are calculated by using the cosmological parameters from the first-year *WMAP* observation ($h = 0.71$, $\Omega_m = 0.27$, $\Omega_\Lambda = 0.73$; Spergel et al. 2003), and a flat universe is assumed. The smoothed line on the spectrum shows the fitted intrinsic flux level, and the solid straight line shows the power-law continuum fit. The vertical dotted lines show the wavelengths of emission lines in the Ly α forest and the low-ionization lines redward of the Ly α emission line. The quasar numbering in Figures 7–11 is the same as in Figure 4 so that we can visualize where the quasar spectrum is in the σ_{i1} versus σ_{i2} diagram. In Table 2, quasars are sorted by classes, and the equivalent width of the emission lines are listed.

5.3. The Characteristics of the Five Classes

The characteristics of the first two PCS directly reflect on the five classifications; thus, let us take a close look at the first two PCS in Figure 2. The first PCS carries the sharp and strong lines: Ly α , Ly β , and high-ionization emission-line features (O VI, N V, Si IV, C IV). The second PCS has low-ionization emission-line features: Fe II and Fe III blueward of the Ly α emission line, Si II and C II redward. Their profiles are broad and rounded. In the second PCS, the flux values of low-ionization emission lines and the strong Ly α and C IV emission lines have opposite sign, meaning that they are anticorrelated. In addition to that, Ly α and C IV emission lines have P Cygni profiles, which introduces asymmetric profiles to these emission lines.

By definition, the first two PCS engage the correlation between emission lines. Since we are particularly interested in the profiles of emission lines in the Ly α forest, let us look at low-ionization lines first. If a quasar shows prominent low-ionization lines redward of the Ly α emission line (Si II $\lambda\lambda 1260$, 1304, C II $\lambda 1334$), it should have a negative second PCS coefficient, and we should expect to have prominent Fe II $\lambda 1070$ and Fe III $\lambda 1123$ in the Ly α forest. Thus, such a quasar should belong to either Class III or IV. As a consequence, these two classes have the largest equivalent widths of these low-ionization lines among the five classes, as seen in Table 2.

If another quasar has sharp and strong Ly α , Ly β , and high-ionization lines (N V, Si IV, C IV), it should have a positive first PCS coefficient and belong to Classes I or IV. The normalized flux of the Ly α emission peak and the ratio of the Ly α and N V peak flux are the highest for Class I among the five classes. We can differentiate Classes I and II, or Classes III and IV by combining the above characteristics. As we expect, the diagonal classes have the opposite characteristics. For example, Class I has sharp and high ionization lines, while Class III has broad and rounded low emission lines.

In practice, the key point of finding the intrinsic flux level in the Ly α forest is to seek the low-ionization lines (Si II $\lambda\lambda 1260$, 1304, C II $\lambda 1334$) and their profiles redward of the Ly α emission. If we see them, we should expect to have similar profiles of Fe II $\lambda 1070$ and Fe III $\lambda 1123$ lines in the Ly α forest. If we do not see them, we can expect the intrinsic flux level to be flat in the Ly α forest and the power-law extrapolation from redward of the Ly α emission to be a good approximation. We will discuss the accuracy of the power-law extrapolation in the next section.

6. MEAN FLUX $\langle F \rangle$ AND FLUX DECREMENT D_A

6.1. A Brief History of the Flux Decrement D_A

Gunn & Peterson (1965) predicted a flux decrement due to foreground neutral hydrogen in the IGM, namely, the Ly α forest. Oke & Korycansky (1982) first defined and measured the flux decrement, D_A . Schneider et al. (1991) introduced the Ly α forest wavelength interval for D_A as $\lambda\lambda 1050$ – 1170 , and it has been widely used since (Zuo & Lu 1993; Kennefick et al. 1995; Spinrad et al. 1998). Madau (1995) and McDonald & Miralda-Escudé (2001) have used D_A to estimate the UV background. The flux decrement of the high-redshift IGM probes the reionization epoch of the universe (Loeb & Barkana 2001). The current estimate of the reionization epoch from the IGM is around $z \sim 6$ – 7 (Becker et al. 2001; Djorgovski et al. 2001; Fan et al. 2003), while the first-year *WMAP* satellite data estimates $z \sim 20$ (Spergel et al. 2003). The discrepancy is yet to be resolved or explained (Cen 2003).

A precise measurement of the flux decrement, D_A , is of great importance for studies of the IGM (Rauch 1998) because it is very sensitive to the cosmological parameters σ_8 (the amplitude of the mass power spectrum) and Ω_Λ , as well as to the UV background intensity (Tytler et al. 2004a; Jena et al. 2005). However, it is this sensitivity that makes the D_A measurement a major source of error (Hui et al. 1999; Croft et al. 2002b).

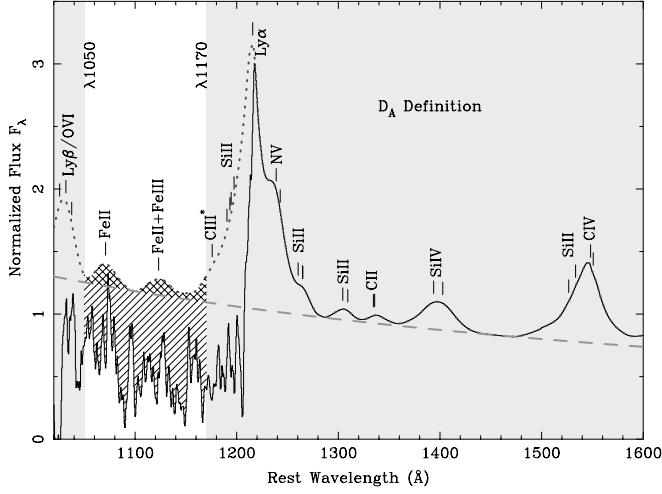


FIG. 6.—Illustration of the D_A definition. The solid line shows the observed $\text{Ly}\alpha$ forest at $z \sim 4.0$ and we artificially imposed on a Class III quasar spectrum. The dotted line represents the intrinsic quasar flux level. The dashed curve shows the power-law extrapolation from redward of the $\text{Ly}\alpha$ emission line. The flux decrement D_A is the fraction of the sum of the hatched and cross-hatched area over the intrinsic flux area in $\lambda\lambda 1050\text{--}1170$. If we use the power-law-extrapolated line, we would miss the cross-hatched area, which is not negligible for the precise measurement. [See the electronic edition of the Supplement for a color version of this figure.]

6.2. The Mean Flux Correction Factor δF

The concept of the following flux decrement D_A and the power-law extrapolation is illustrated in Figure 6. The flux decrement is defined as

$$D_A = 1 - \frac{\int_{1050 \text{ \AA}}^{1170 \text{ \AA}} f_\lambda(\lambda; \text{Observed}) d\lambda}{\int_{1050 \text{ \AA}}^{1170 \text{ \AA}} f_\lambda(\lambda; \text{Quasar}) d\lambda}. \quad (15)$$

Thus, what we are measuring is the mean flux:

$$\langle F \rangle = \frac{\int_{1050 \text{ \AA}}^{1170 \text{ \AA}} f_\lambda(\lambda; \text{Observed}) d\lambda}{\int_{1050 \text{ \AA}}^{1170 \text{ \AA}} f_\lambda(\lambda; \text{Quasar}) d\lambda}. \quad (16)$$

However, the unabsorbed-intrinsic quasar flux level is not seen in the $\text{Ly}\alpha$ forest and the power-law extrapolation from redward of $\text{Ly}\alpha$ emission has been used as a background flux level. In fact, what is reported in the literature as the mean flux is

$$\langle F_{\text{power-law}} \rangle = \frac{\int_{1050 \text{ \AA}}^{1170 \text{ \AA}} f_\lambda(\lambda; \text{Observed}) d\lambda}{\int_{1050 \text{ \AA}}^{1170 \text{ \AA}} f_\lambda(\lambda; \text{Power-law}) d\lambda}, \quad (17)$$

which is not exactly the same as $\langle F \rangle$, since the power law is a crude approximation of the continuum in the $\text{Ly}\alpha$ forest, as we have seen in § 5, the Appendix, and Figures 7–11.

We wish to introduce a correction factor δF ,

$$\delta F = \frac{\int_{1050 \text{ \AA}}^{1170 \text{ \AA}} f_\lambda(\lambda; \text{Power-law}) d\lambda}{\int_{1050 \text{ \AA}}^{1170 \text{ \AA}} f_\lambda(\lambda; \text{Quasar}) d\lambda}, \quad (18)$$

so that we can estimate the true mean flux $\langle F \rangle$ from the reported mean flux $\langle F_{\text{power-law}} \rangle$:

$$\langle F \rangle = \langle F_{\text{power-law}} \rangle \delta F. \quad (19)$$

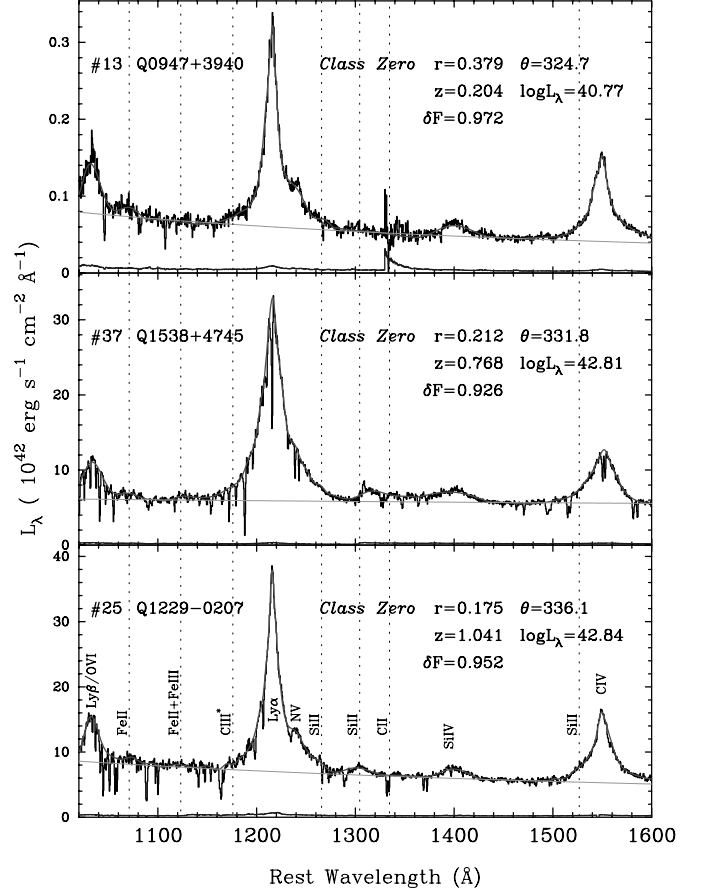


FIG. 7.—Class Zero ($r \leq 0.668$): The smooth line on the spectrum shows the fitted continuum, and the straight solid line shows the power-law continuum fit. The line at the bottom is the 1σ error of the spectrum. The vertical dotted lines show the wavelengths of emission lines in the $\text{Ly}\alpha$ forest and low-ionization lines redward of the $\text{Ly}\alpha$ emission line. The luminosity, L_λ , is measured at $\lambda 1280$, where we normalized the spectra. The emission lines in the $\text{Ly}\alpha$ forest are barely seen in the three spectra. A discontinuity of the spectrum is seen in the middle of the spectrum in Q0947+3940 and Q1538+4745. These are due to the different gratings used in the observations to cover the wide range of wavelengths. We joined them together by taking the weighted mean, but it does not always give a smooth solution. This discontinuity could be another source of fitting errors. [See the electronic edition of the Supplement for a color version of this figure.]

To calculate δF , we need to find the power-law extrapolation from the redward $\text{Ly}\alpha$ emission. Since our wavelength range is limited and not as large as other survey data, it is not easy to extrapolate. Moreover, we have a series of emission lines, and it is hard to define an intrinsic flux level with no emission lines. For example, as shown in Figure 10, Class III quasars have emission lines throughout this wavelength range. However, we have a fitted intrinsic flux level in the $\text{Ly}\alpha$ forest, and we take advantage of it. We choose two points and find a power-law fit that runs through these two points. We choose one from blueward ($\lambda 1100$) and the other from redward ($\lambda 1450$) of the $\text{Ly}\alpha$ emission. Then we can have an interpolated and extrapolated power-law continuum and its exponent α_ν , for $f_\nu \propto \nu^{\alpha_\nu}$. The average of α_ν is -0.854 with a standard deviation of 0.507 . The power-law continua show that they are all sensible first-order approximations that well represent the intrinsic flux levels in the $\text{Ly}\alpha$ forest. The power-law continua are shown in Figures 7–11.

The calculated δF is listed in Table 2 and the average of δF is 0.947 , with a standard deviation of 0.031 . This result means that the power-law approximation misses 5.3% of the flux from the quasar in the D_A wavelength range and proves that the power-law

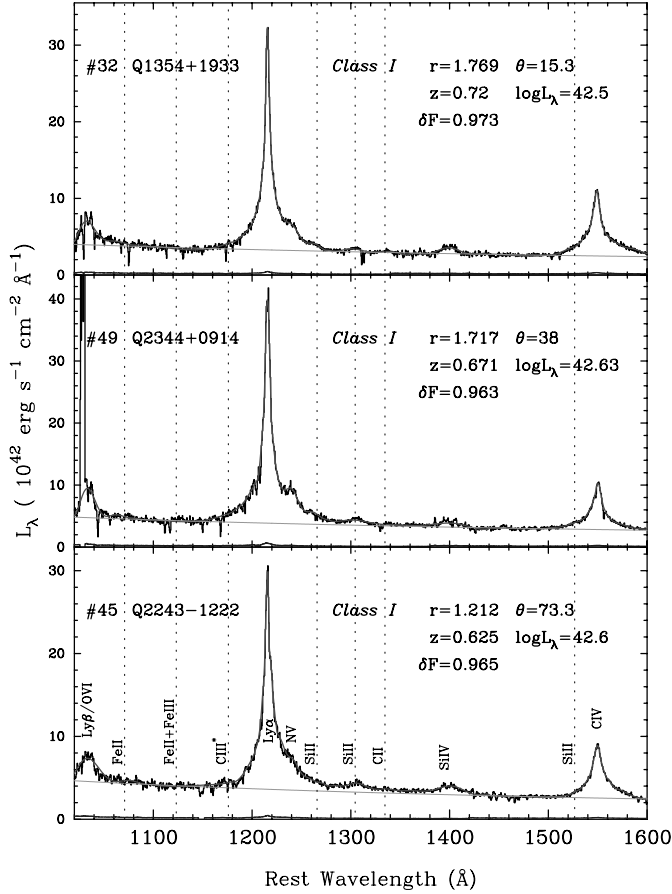


FIG. 8.—Class I ($r > 0.668$, $0 \leq \theta < 90^\circ$): The Ly α , Ly β , and high-ionization emission lines are all very sharp and in high contrast with the continuum. The low-ionization lines, Si II at $\lambda\lambda 1260, 1304$, are barely seen. We see no clear sign of emission lines in the Ly α forest, and the power-law continuum is a good approximation. The contrast of the Ly α emission peak with the continuum is the highest among the five classes. In Q2344+0914, there is a huge spike at 1030 Å. It is due to an emission line caused by Earth's atmosphere. We removed these spikes when we fitted the continuum. [See the electronic edition of the Supplement for a color version of this figure.]

approximation is inadequate to perform a D_A measurement that attempts 1% accuracy (Tytler et al. 2004b; Jena et al. 2005). The distribution of δF is shown in Figure 12, and it is not a Gaussian. The PDF of δF is asymmetric and has a long tail toward small δF values.

There are two major reasons for the missing flux. The first reason is that the D_A wavelength range is still in the tail of the prominent Ly β /O VI and Ly α emission lines. For example, the blueward tail of the Ly α emission starts near $\lambda 1160$, which is 10 Å below the $\lambda 1170$ upper limit of D_A wavelength range. The effect from the tails of Ly β and Ly α emission is common for all of the quasars, as we can see in Figures 7–11. This contribution is about 4%–5%, and we always miss this fraction of the flux, which means that δF is always less than unity.

The second reason is the contribution from the weak emission lines in the Ly α forest. The intrinsic flux level at the emission lines is naturally above the power-law extrapolation; therefore, we would always expect to miss flux from the emission lines, making δF always less than unity. The low-ionization emission lines in the Ly α forest are prominent for Class III and Class IV quasars. Four quasars in Classes III and IV have values of δF less than 0.9, meaning that we miss more than 10% of the flux if we use power-law extrapolation. The quasar that has the smallest δF , 0.86, is Q1544+4855. This quasar is shown in the top panel

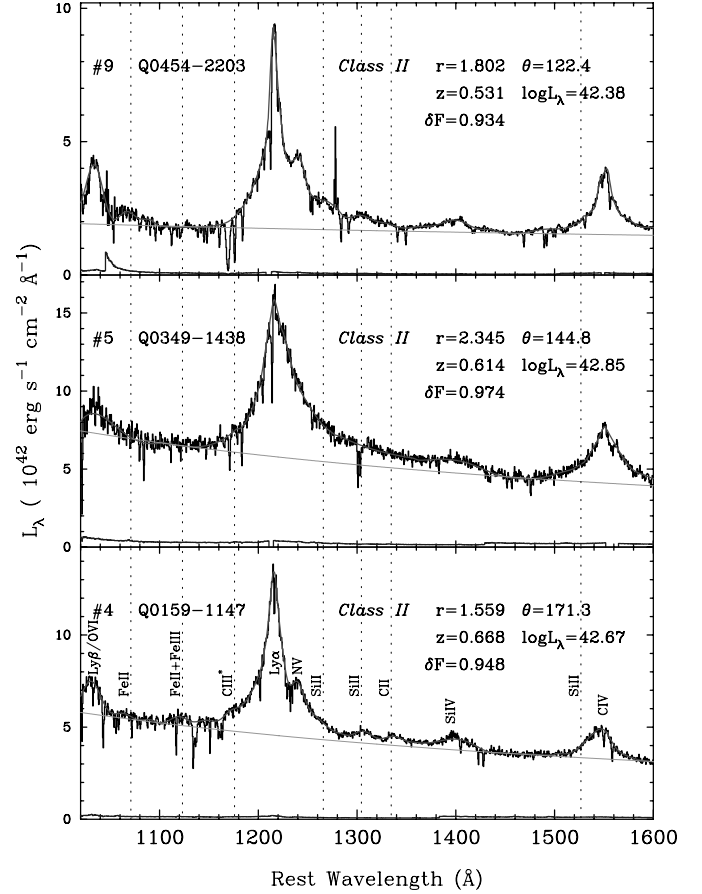


FIG. 9.—Class II ($r > 0.668$, $90^\circ \leq \theta < 180^\circ$): The Ly α emission peak has a moderate contrast, 4–6, with the continuum, and the emission peak ratio of Ly α and N V is 2–3. The Ly α emission has long tails, and the blueward tail of the fitted continuum does not meet with the power-law continuum until 1120 Å, which is 50 Å below the D_A wavelength definition, 1170 Å. In an extreme case, Q0349–1438 ($r = 2.345$), the tail of Ly α emission wings last about 100 Å. Ly β /O VI, Ly α , and C IV emission profiles are triangular, and Si IV $\lambda 1393$ is very broad and rounded. There is no clear separation between Ly α and N V emission lines and no sign of low-ionization emission lines. [See the electronic edition of the Supplement for a color version of this figure.]

of Figure 11, and the power-law continuum fit looks sensible. Together with the tails of Ly β and Ly α emissions, the low-ionization emission lines in the Ly α forest (Fe II, Fe III) contribute 14% of the flux, which is significant and should not be neglected.

There is another possible origin for the missing flux. We might have a global change of an intrinsic quasar flux level. Shang et al. (2005) showed that there exists a variety of UV spectrum shape in a global scale, known as the big blue bump. We think that this big blue bump is due to the thermal radiation of the accretion disk near the supermassive black hole (Malkan 1983), and spectral shape varies quasar by quasar (Sun & Malkan 1989). However, we found a moderate correlation between the intrinsic flux levels and the emission profiles in Paper I, and we expect that the global trend is imprinted in the PCS. In addition to that, the wavelength range of the D_A measurement is relatively small compared to the global change of the slope, so we expect the effect is minimal. But we need to have a quantitative study, and we note that this slope change could be the source of systematic errors.

We expect that we need to apply at least a $\delta F = 0.947$ correction to the D_A measurements in the literature. The discrepancy between the past D_A measurements and those of Bernardi et al. (2003) using the weak emission profile fitting method is shown

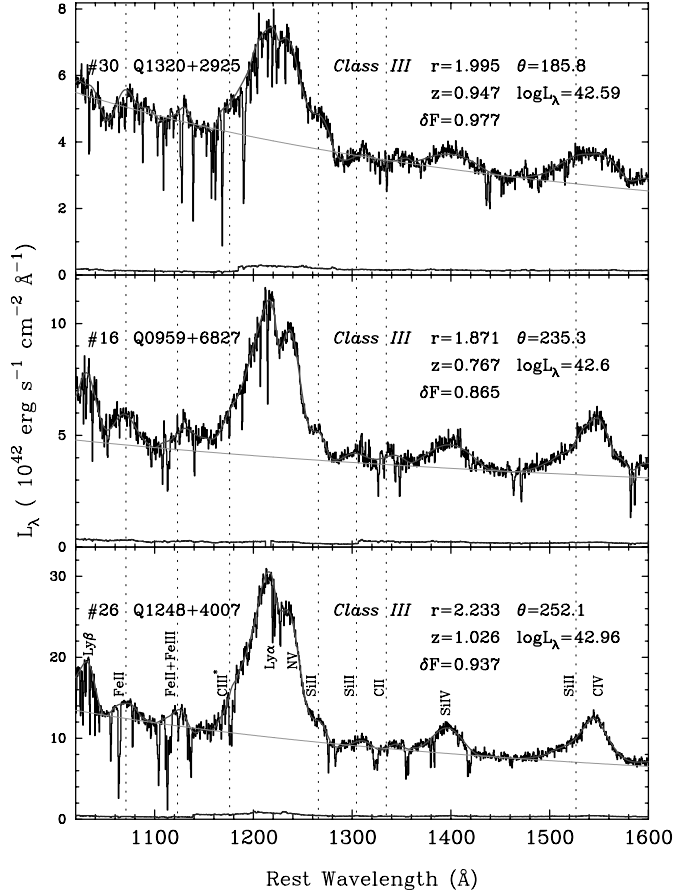


FIG. 10.—Class III ($r > 0.668$, $180^\circ \leq \theta < 270^\circ$): The emission-line profiles are all broad and rounded. Fe II and Fe III lines are clearly seen in the Ly α forest. The contrast of the Ly α emission-line peak with the continuum is the lowest, 2–4, among the five classes. The ratio of Ly α emission peak to N V is also the lowest: 1–2. The C IV profile is asymmetric, probably because of the contribution from the Si II λ 1526 hidden inside the blueward tail of the C IV line. [See the electronic edition of the Supplement for a color version of this figure.]

in Figure 22 of Tytler et al. (2004b). The disagreement is approximately 5% at redshift $2 < z < 3$, and in terms of the mean flux, the power-law-fitted values (Press et al. 1993; Steidel & Sargent 1987) are always above that of profile-fitted ones (Bernardi et al. 2003). The correction factor, $\delta F = 0.947$, explains this disagreement well.

However, we expect that δF changes with redshift, and it is crucial to include the effect from the weak emission lines to investigate the reionization epoch. Known as the Baldwin effect (Baldwin 1977), the emission profile of lines, such as C IV, and the luminosity of the quasar are correlated. Because of the anti-correlation between the equivalent width of C IV and the luminosity, we expect Class III quasars to be the brightest since they have the smallest C IV equivalent width. Due to the selection effect, we would expect to observe the brightest quasars at high redshifts. Therefore, the fraction of classes for the observed quasars should change with redshift. In fact, the highest redshift quasars reported by Fan et al. (2001), Becker et al. (2001), and Djorgovski et al. (2001) probably belong to Class III, because they all show the weak Si II λ 1304 emission line which implies that they have weak emission lines in the Ly α forest region. J104433.04–012502.2 ($z = 5.80$) and J08643.85+005453.3 ($z = 5.82$) definitely belong to Class III since they have broad Ly α , N V, and Si II emission lines and a low Ly α /N V emission intensity ratio. The mean flux correction δF of Class III quasars

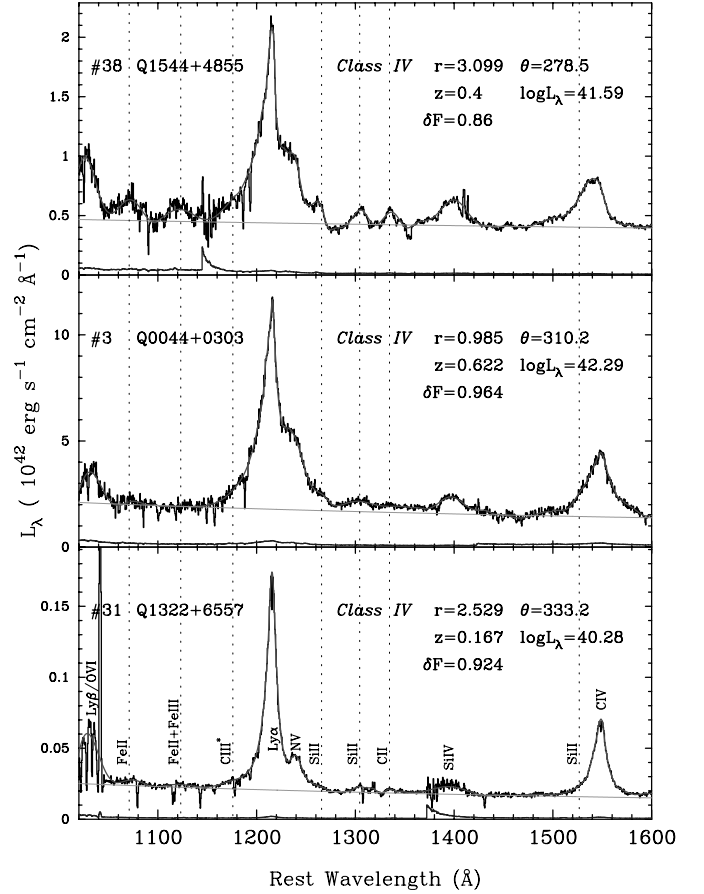


FIG. 11.—Class IV ($r > 0.668$, $270^\circ \leq \theta < 360^\circ$): The high contrast with the continuum and sharp emission profile are the characteristics of this class. Q1544+4855 is an extreme case that has $r = 3.099$. Since it has $\theta = 278.5^\circ$, it is very close to Class III, but it has the characteristics of Class IV: high Ly α emission-line peak contrast and the very sharp line profiles. Unlike a Class III quasar, the peaks of the low-ionization line profile are very sharp and not rounded. Q1322+6557 has a spike at λ 1040 that is due to an atmospheric emission line. The fitted spectrum removed the spike for analysis. [See the electronic edition of the Supplement for a color version of this figure.]

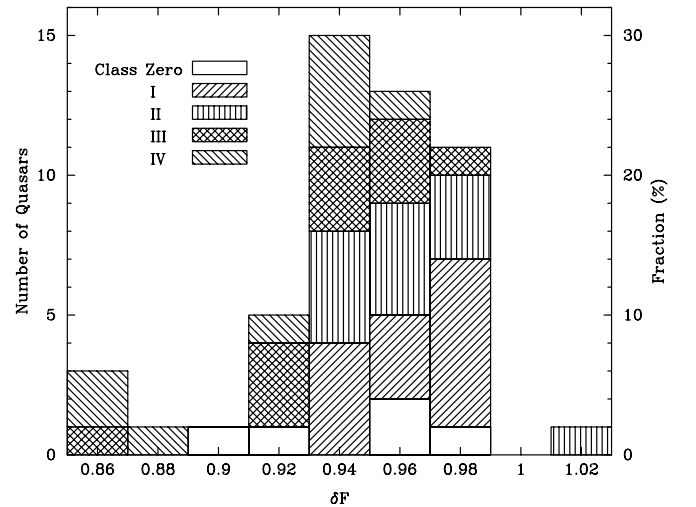


FIG. 12.—Distribution of the mean flux correction factor δF . The mean is 0.947, and the standard deviation is 0.031. The distribution is asymmetric with a long tail toward small δF values. Class III and IV quasars have prominent emission lines in the Ly α forest and tend to have small δF values. Two extreme spectra for low δF are shown in Fig. 10 for Q0959+6927 and Fig. 11 for Q1544+4855. [See the electronic edition of the Supplement for a color version of this figure.]

are in the range of 0.91–0.97, meaning that the power-law extrapolation misses 3%–9% of the flux for Class III quasars. We note that the reported 1σ error of the residual mean flux at redshift $z = 5.75$ by Becker et al. (2001) is 0.03. The contribution from δF is bigger than their claimed error, and it is systematic. This correction would bring the observed mean flux down by 3%–9% percent and would bring D_A up by the same fraction. Therefore, it is crucial to take into account the δF correction in order to investigate the reionization epoch.

7. SUMMARY

We analyzed the wide variety of the emission-line profiles in the Ly α forest both in a quantitative and qualitative way. We used PCA to describe the variety of quasar spectra, and we found that 1161 pixels of data ($\lambda\lambda 1020$ – 1600 with 0.5 \AA binning) can be summarized by the primary seven PCS coefficients because the pixels are not independent but are strongly correlated with each other. We presented, for the first time, the idea of generating artificial quasar spectra. Our artificial quasar spectra should be useful in testing the detections, in calibrations, and in simulations. We introduced five classes to differentiate the families of quasar spectra and showed how the classification can guide us to find the intrinsic flux level in the Ly α forest. It is essential to account for emission-line features in the Ly α forest to perform a precise measurement of the mean flux in order to probe cosmological parameters, the UV background, and the reionization epoch; otherwise, on average, the commonly used power-law extrapolation continuum misses 5.3% of the flux, and we have found cases in which it misses up to 14% of the flux.

To investigate the high-redshift Ly α forest, we showed the need to account for the emission lines in the Ly α forest. An

emission-line profile-oriented continuum fitting method by Bernardi et al. (2003), or improvement of the PCA method in Paper I, would be useful for a large data set such as the Sloan Digital Sky Survey. If we can study the redshift evolution of the quasar spectra and if we can estimate the constituents of classes at a certain redshift, we would be able to estimate the mean flux statistically using the mean flux correction factor δF . For precision cosmology, the formalisms we presented here should play an important role.

I thank Regina Jorgenson, Kim Griest, Jeff Cooke, Carl Melis, Tridi Jena, and Geoffrey So for their careful reading of this manuscript and encouragements. I thank David Tytler and David Kirkman for the comments on the manuscript and the discussions on the Ly α forest studies. I also thank Dan Lubin for helping me to establish the *HST* database. I thank Art Wolfe and Chris Hawk for the discussions on the emission line identifications. I would like to thank the anonymous referee for constructive comments on the manuscript. I am grateful to Paul Francis, who provided the code and LBQS spectra. Paul Hewett kindly sent the error arrays for those spectra. Wei Zheng and Buell Januzzi kindly provided copies of *HST* QSO spectra that we used before we located the invaluable collection of *HST* spectra posted to the Web by Jill Bechtold. I thank the Okamura Group at the University of Tokyo from whom I learned the basics of PCA. I thank the hospitality of Shin-ichi Ichikawa and the support of Chie Naito at the Astronomical Data Analysis Center of the NAOJ. This work was supported in part by NASA grants NAG5-13113 and HST-AR-10288.01-A from the STScI and by NSF grant AST 00-98731.

APPENDIX

WEAK EMISSION LINES IN THE Ly α FOREST

It has been suggested that there exist weak emission lines in the Ly α forest (Zheng et al. 1997; Telfer et al. 2002; Bernardi et al. 2003; Scott et al. 2004); however, their identities, strengths, and line profiles are not well understood. More importantly, we wish to know how they are correlated with other emission lines so that we can predict the strength and profiles of the emission lines in the Ly α forest. We attempt to find the identities of the three weak emission lines in the Ly α forest reported by Tytler et al. (2004a). In this paper, we use their measured wavelengths: $\lambda = 1070.95$, 1123.17 , and 1175.88 \AA .

A1. LINE AT $\lambda = 1070.95\text{ \AA}$: Fe II

Zheng et al. (1997) and Vanden Berk et al. (2001) identified this line as Ar I $\lambda 1066.66$, but the contribution from Ar I cannot be this large. The Ar I line has another transition at $\lambda 1048.22$, whose transition probability ($A_{ik} = 4.94 \times 10^8\text{ s}^{-1}$) is stronger than that of $\lambda 1066.66$ ($A_{ik} = 1.30 \times 10^8\text{ s}^{-1}$). However, there is no clear sign of the $\lambda 1048.22$ line feature in 50 *HST* spectra or 79 quasar spectra in Tytler et al. (2004b). In addition, the $\lambda 1070$ line has a broad and asymmetric profile, which suggests that this line is a blend of multiple lines. Thus, $\lambda 1070$ is not likely to be a single Ar I line.

Telfer et al. (2002) labeled this $\lambda 1070$ as the N II + He II line and mentioned S IV as a possible candidate. Scott et al. (2004) identify four lines in the proximity of this wavelength: the S IV doublet ($\lambda\lambda 1062, 1073$) and N II + He II + Ar I ($\lambda 1084$). As we have seen in § 5, the $\lambda 1070$ line correlates with low-ionization lines such as Si II and C II. S IV does not fit into this category. N II seems to be a good candidate, but the N II lines peak around 1085 \AA , which is 15 \AA away from what we see. It is unlikely that we have 15 \AA of wavelength error. For the same reason, He II (1085 \AA), a high-ionization line, is not likely to be the dominant contributor. However, it is reasonable to expect to have an He II line, since He II $\lambda 1640$ is often seen in quasar spectra. This $\lambda 1070$ line is seen in the Q1009+2956 and Q1243+3047 spectra for which we have high S/N Keck HIRES spectra with a $\text{FWHM} = 0.0285\text{ \AA}$ resolution at this wavelength (Burles & Tytler 1998; Kirkman et al. 2003). If $\lambda 1070$ is comprised of the lines suggested by Scott et al. (2004), we would be able to resolve the individual lines. However, none of the individual emission lines are resolved. This fact implies that this emission line is comprised of numerous weak lines and that they are probably low-ionization lines because of the good correlation with other low-ionization lines.

Fe II suits such a description, and in fact, Fe II has a series of UV transitions around this wavelength range: $\lambda\lambda 1060$ – 1080 . However, we do not see other expected Fe II emission lines. If this $\lambda 1070$ is Fe II, we would expect to see the Fe II UV10 multiplet around $\lambda 1144$, which is supposed to be stronger than the $\lambda 1070$ line. But no sign of an emission line is seen at that wavelength. Therefore, the Fe II identification may be wrong, or there may be a mechanism that we are not aware of that prevents the expected $\lambda 1144$ emission line.

A2. $\lambda = 1123.17 \text{ \AA}$: Fe II + Fe III

Telfer et al. (2002); Vanden Berk et al. (2001) identify $\lambda 1123$ as Fe III. The f -value weighted Fe III UV1 multiplet has a wavelength at 1126.39 \AA , which is very close to what was observed by Tytler et al. (2004b). The distribution of the multiplet lines matches the broad $\lambda 1123$ feature found in quasars. There are no other major resonance lines in this wavelength range except C I. In the wavelength range $\lambda 1114\text{--}1200$, C I has a series of lines, and there exist stronger lines redward of the Ly α emission line: $\lambda 1115\text{--}1193$, $\lambda 1277\text{--}1280$. However, we do not see these redward C I emission lines, and there is no sign of correlation between $\lambda 1123$ and these possible lines (Paper I). Thus, $\lambda 1123$ is probably Fe III. In addition to Fe III, Fe II also has UV11–14 multiplets around this wavelength: $\lambda 1121\text{--}1133$. Given the fact that this $\lambda 1123$ line is well correlated with the $\lambda 1070$ line, it is reasonable to expect to see Fe II lines here as well, if the identification of $\lambda 1070$ is Fe II.

A3. $\lambda = 1175.88 \text{ \AA}$: C III*

Telfer et al. (2002) and Vanden Berk et al. (2001) identified $\lambda 1175$ as C III*, although as shown in Table 2, we do not have a clear detection of this line because it is being a weak and narrow feature. We can see the $\lambda 1175$ line in the *HST* composite spectrum (Telfer et al. 2002), the SDSS composite spectrum (Vanden Berk et al. 2001), and in 11 out of 79 quasar spectra in Tytler et al. (2004b). Therefore, we are confident that this $\lambda 1175$ is a real emission line. The f -value weighted wavelength of the C III* line is $\lambda 1175.5289$, which matches well with the observed wavelength. There is no major resonance line at this wavelength.

A4. OTHER POSSIBLE EMISSION LINES IN THE Ly α FOREST

Tytler et al. (2004a) and Telfer et al. (2002) reported observing the Si II $\lambda 1195$ line in their spectra. We do not have any clear detection of the Si II $\lambda 1195$ line in the 50 quasar spectra. Since other Si II lines, $\lambda 1265$, 1304 , are clearly seen redward of the Ly α emission line, it is plausible to expect the Si II $\lambda 1195$ line.

Si III has a transition at $\lambda 1206.50$. Since we see both Si II and Si IV redward of Ly α emission, it is natural to expect to see Si III. However, no detection is reported in the literature, and we do not have any positive detection in the 50 quasar spectra. The Si III $\lambda 1206$ emission line is probably too weak or possibly overwhelmed by broad Ly α emission, only 10 \AA away, whose equivalent width is often greater than 100 \AA .

REFERENCES

- Bahcall, J., et al. 1993, *ApJS*, 87, 1
 ———. 1996, *ApJ*, 457, 19
 Baldwin, J. A. 1977, *ApJ*, 214, 679
 Bechtold, J., et al. 2002, *ApJS*, 140, 143
 Becker, R. H., et al. 2001, *AJ*, 122, 2850
 Bernardi, M., et al. 2003, *AJ*, 125, 32
 Boroson, T. A. 2002, *ApJ*, 565, 78
 Boroson, T. A., & Green, R. F. 1992, *ApJS*, 80, 109
 Burles, S., & Tytler, D. 1998, *ApJ*, 507, 732
 Cabanac, R. A., de Lapparent, V., & Hickson, P. 2002, *A&A*, 389, 1090
 Cen, R. 2003, *ApJ*, 591, 12
 Connolly, A. J., Szalay, A. S., Bershad, M. A., Kinney, A. L., & Calzetti, D. 1995, *AJ*, 110, 1071
 Croft, R. A. C., Hernquist, L., Springel, V., Westover, M., & White, M. 2002a, *ApJ*, 580, 634
 Croft, R. A. C., Weinberg, D. H., Bolte, M., Burles, S., Hernquist, L., Katz, N., Kirkman, D., & Tytler, D. 2002b, *ApJ*, 581, 20
 Djorgovski, S. G., Castro, S., Stern, D., & Mahabal, A. A. 2001, *ApJ*, 560, L5
 Fan, X., et al. 2001, *AJ*, 122, 2833
 ———. 2003, *AJ*, 125, 1649
 Francis, P. J., Hewett, P. C., Foltz, C. B., & Chaffee, F. H. 1992, *ApJ*, 398, 476
 Gunn, J. E., & Peterson, B. A. 1965, *ApJ*, 142, 1633
 Hewett, P. C., Foltz, C. B., & Chaffee, F. H. 1995, *AJ*, 109, 1498
 ———. 2001, *AJ*, 122, 518
 Hui, L., Stebbins, A., & Burles, S. 1999, *ApJ*, 511, L5
 Jannuzi, B., et al. 1996, *ApJ*, 470, L11
 Jena, T., et al. 2005, *MNRAS*, 361, 70
 Karhunen, K. 1947, *Ann. Acad. Sci. Fenn. A*, 1, 37
 Kendall, M. G. 1980, *Multivariate Analysis* (London: Griffin)
 Kenefick, J. D., Djorgovski, S. G., & de Carvalho, R. R. 1995, *AJ*, 110, 2553
 Kirkman, D., Tytler, D., Suzuki, N., O'Meara, J. M., & Lubin, D. 2003, *ApJS*, 149, 1
 Loeb, A., & Barkana, R. 2001, *ARA&A*, 39, 19
 Loève, M. 1948, *Processus Stochastiques et Mouvement Brownien* (Paris: Hermann)
 Madau, P. 1995, *ApJ*, 441, 18
 Malkan, M. A. 1983, *ApJ*, 268, 582
 McDonald, P., & Miralda-Escudé, J. 2001, *ApJ*, 549, L11
 Morton, D. C. 1991, *ApJS*, 77, 119
 Oke, J. B., & Korycansky, D. G. 1982, *ApJ*, 255, 11
 Press, W. H., Rybicki, G. B., & Schneider, D. P. 1993, *ApJ*, 414, 64
 Rauch, M. 1998, *ARA&A*, 36, 267
 Sakurai, J. J. 1985, *Modern Quantum Mechanics* (Boston: Addison Wesley)
 Schneider, D. P., Schmidt, M., & Gunn, J. E. 1991, *AJ*, 101, 2004
 Scott, J. E., et al. 2004, *ApJ*, 615, 135
 Shang, Z., et al. 2005, *ApJ*, 619, 41
 ———. 2003, *ApJ*, 586, 52
 Spergel, D. N., et al. 2003, *ApJS*, 148, 175
 Spinrad, H., et al. 1998, *AJ*, 116, 2617
 Steidel, C. C., & Sargent, W. L. W. 1987, *ApJ*, 313, 171
 Sun, W., & Malkan, M. A. 1989, *ApJ*, 346, 68
 Suzuki, N., Tytler, D., Kirkman, D., O'Meara, J. M., & Lubin, D. 2003, *PASP*, 115, 1050
 ———. 2005, *ApJ*, 618, 592 (Paper I)
 Telfer, R. C., Zheng, W., Kriss, G. A., & Davidsen, A. F. 2002, *ApJ*, 565, 773
 Tytler, D., O'Meara, J. M., Suzuki, N., Kirkman, D., Lubin, D., & Orin, A. 2004a, *AJ*, 128, 1058
 Tytler, D., et al. 2004b, *ApJ*, 617, 1
 Vanden Berk, D. E., et al. 2001, *AJ*, 122, 549
 Yip, C. W., et al. 2004, *AJ*, 128, 2603
 Zheng, W., Kriss, G. A., Telfer, R. C., Grimes, J. P., & Davidsen, A. F. 1997, *ApJ*, 475, 469
 Zuo, L., & Lu, L. 1993, *ApJ*, 418, 601